PHYSICAL REVIEW MATERIALS **1**, 024801 (2017)

Probing localized strain in solution-derived $YBa_2Cu_3O_{7-\delta}$ nanocomposite thin films

Roger Guzman,[*] Jaume Gazquez, Bernat Mundet, Mariona Coll, Xavier Obradors, and Teresa Puig
Institut de Ciència de Materials de Barcelona, ICMAB-CSIC, Campus de la UAB, 08193 Bellaterra, Spain

(Received 5 April 2017; published 12 July 2017)

Enhanced pinning due to nanoscale strain is unique to the high-T_c cuprates, where pairing may be modified with lattice distortion. Therefore a comprehensive understanding of the defect landscape is required for a broad range of applications. However, determining the type and distribution of defects and their associated strain constitutes a critical task, and for this aim, real-space techniques for atomic resolution characterization are necessary. Here, we use scanning transmission electron microscopy (STEM) to study the atomic structure of individual defects of solution-derived $YBa_2Cu_3O_7$ (YBCO) nanocomposites, where the inclusion of incoherent secondary phase nanoparticles within the YBCO matrix dramatically increases the density of $Y_1Ba_2Cu_4O_8$ (Y124) intergrowths, the commonest defect in YBCO thin films. The formation of the Y124 is found to trigger a concatenation of strain-derived interactions with other defects and the concomitant nucleation of intrinsic defects, which weave a web of randomly distributed nanostrained regions that profoundly transform the vortex-pinning landscape of the YBCO nanocomposite thin films.

DOI: 10.1103/PhysRevMaterials.1.024801

I. INTRODUCTION

Oxide-based nanocomposites form a new and yet very incomplete area of research, as there is more to be known about the relationships between functionality, nanocomposite microstructure, strain, and composition modulations at the nanoscale. Indeed, the primary limitation on exploitation is the difficulty of achieving sufficient precise control of the properties because of the range of possible defects in such materials, and the remarkably strong effect of such defects on their properties. A paradigmatic case is the high T_c superconductor $YBa_2Cu_3O_7$ (YBCO), the performance of which is dictated by a subtle interplay of a variety of nanoscale defect structures that pin the magnetic flux lattice and thus prevent resistive current flow [1–4]. Accordingly, in recent years, tremendous efforts have been made towards the nanoengineering of YBCO films, consisting of the assembly of nonsuperconducting phases within the YBCO matrix, which have rendered enhanced performance [3–11]. However, the localization of the vortices' core at insulating regions, provided their dimension is in the range of the coherence length ξ, is not the only effective vortex-pinning mechanism. Recent results pointed out the possibility that the Cooper pair formation might be quenched under tensile strain, therefore forming a new and effective pinning mechanism in high-temperature superconductors [12,13].

Here we will describe in detail the structural defect landscape of solution-derived YBCO nanocomposites with Ba_2YTaO_6 (BYTO) as a prototype example of secondary phase nanoparticles. Compared to other growing techniques, the microstructure of solution-based nanocomposites changes drastically due to the specifics of the chemical solution deposition technique (CSD). By the efficient introduction of a variety of selected nonsuperconducting nanosized secondary species in the YBCO matrix, solution-derived nanocomposites have been shown to deeply transform the materials' microstructure yielding an enhancement of the superconducting properties [3,13–24]. In the YBCO-BYTO nanocomposite system, the nucleation of secondary phases occurs prior to the growth of YBCO frustrating an epitaxial relationship of the nanoinclusions with YBCO (incoherent interfaces) and bringing forth the highest fraction of randomly oriented nanoparticles enabled by the large lattice in-plane mismatch with YBCO ($\varepsilon = 8.5\%$). Certainly, only those near the substrate interface maintain a clear epitaxial order [21,25]. In particular, YBCO-BYTO nanocomposites present a highly defective microstructure and a strong enhancement of the vortex pinning that has been attributed to nanostrain [13,21], i.e., elastic distortions of the crystal lattice at the atomic scale, evidencing the need to control and tune the type of defects and their density and distribution. Optimized films (YBCO with 6 mol% BYTO) show an overall improvement of the isotropic pinning contribution with J_c of 4–5 $\mathrm{MA\,cm^{-2}}$ and pinning forces, F_p max, of 6 $\mathrm{GN\,m^{-3}}$ at 77 K (see Refs. [21,25]).

Although all these structural defects are present in pristine YBCO layers, their density and distribution is strongly modified due to the shape, size, orientation, and spreading of the embedded nanoparticles [6,13,21,26]. Here, we have used aberration-corrected scanning transmission electron microscopy (STEM) to unveil the complexity of the defect landscape of these YBCO nanocomposites. Combining high-angle annular dark field (HADDF), low-angle annular dark field (LAADF) imaging modes, and local strain analyses, we have been able to map and quantify the lattice deformations associated to the defects. The resulting complex defect landscape yields a disordered three-dimensional inhomogeneous nanostrain that affects and enhances the physical properties of these nanocomposites, leading to the unique quasi-isotropic vortex pinning behavior of the YBCO nanocomposites.

II. EXPERIMENTAL METHODS

Chemical solution deposited 250-nm YBCO-BYTO thin films were prepared on (100) $LaAlO_3$ (LAO) single-crystal

---

[*] roger.guzman.aluja@gmail.com

substrates from a trifluoroacetate (TFA) precursor solution of Y, Ba, and Cu containing stoichiometric amounts of tantalum (V) ethoxide for 6% mol BYTO in YBCO films. Solution deposition, standard growth and oxygenation conditions have been described elsewhere [21]. Cross-sectional STEM specimens were prepared by conventional mechanical polishing and low-voltage Ar^+ ion milling for the final thinning. Aberration-corrected STEM analyses were carried out in a probe-corrected FEI Titan 60–300 microscope operated at 300 kV, fitted with a high-brightness field-emission gun (X-FEG) and a CEOS probe Cs corrector. Atomic-resolution Z contrast images were obtained by HAADF imaging in STEM, with a convergence angle of 25 mrad and a probe size below 1 Å. The HAADF-STEM images were acquired using an annular detector of which solid angle was conditioned in the range from 58 to 200 mrad, while the LAADF-STEM images in the range from 25 to 58 mrad.

III. RESULTS AND DISCUSSION

Extensive transport critical-current-density measurements showed a strong enhancement of the pinning force as well as an isotropic pinning behavior in a wide range of temperatures up to 77 K in the YBCO-BYTO nanocomposites [21,25,27], indicating a substantial different defect landscape when compared with a pristine YBCO thin film. The best way to visualize the complex microstructure of solution-based YBCO films is using an aberration corrected STEM, as it is able to provide multiple signals simultaneously. In STEM the most used imaging mode is the HAADF, in which an annular detector with a large inner collection angle (typically $\theta >$ 60 mrad) is placed in a way that the diffraction contrast is excluded from the STEM signal and the contrast only ensues from the high angle scattering strength, giving rise to the so called Z-contrast imaging [28]. Simultaneously, electrons scattered to lower angles can be also collected using a smaller collection angle (20 to 60 mrad), which can result in an image with enhanced contrast from defects [29–31]. The defects cause distortions of the lattice in such a way that lead to a dechanneling of the incident electron beam [32]. When the electron beam is scanned over a distorted lattice the electron scattering results in different angular distributions and the intensity collected by the ADF detector from the strained region can be different than that from the strain-free region thus causing extra contrast. Then, the combination of both high-angle with low-angle ADF is an easy and straightforward method to visualize the nanoscale lattice deformations present in the YBCO matrix associated to defects and nanoparticles. Figures 1(a) and 1(b) show the simultaneously acquired HAADF and LAADF images, respectively, of a YBCO with 6% mol BYTO nanocomposite film showing a very high density of defects as well as a homogeneous distribution of BYTO nanoparticles both at the matrix and interface. In HAADF, the dark stripes running parallel to the (001) YBCO plane evidence the presence of planar defects in the film, Fig. 1(a). However, these planar defects appear brighter in LAADF as well as the YBCO areas of the film with a high concentration of them, Fig. 1(b). As expected, defect-free areas present a homogenous darker contrast in LAADF, just as the substrate. The aforementioned defects correspond to the common and well known $Y_1Ba_2Cu_4O_8$ (Y124) structural defect, which consist of an intergrowth of an extra Cu-O chain layer inserted into the YBCO structure [13,33–37]. The presence of this extra Cu-O layer involves a nonconservative stacking fault with a displacement vector $[0, b/2, c/6]$ being the two parts of the structure on either side of the fault laterally shifted over ½b when viewed along the $[100]_{\mathrm{YBCO}}$ direction [38]. When this double Cu-O layer occurs as a single layer with a finite lateral extent, it is structurally analogous to a Frank loop dislocation, i.e., an extrinsic stacking fault surrounded by a partial dislocation that induces a lattice deformation on the surrounding YBCO. The irregular bright (dark) contrast observed along the intergrowths in the LAADF (HAADF) images must be attributed to the presence of the recently observed point defects within the double chain, which are randomly distributed and consist of two Cu vacancies accompanied with three O vacancies [39]. The presence of these complex point defects prevents a local off-stoichiometry, as the Y124 intergrowth involves an extra Cu-O chain. The particular lattice distortions associated to these defects will be addressed later on.

Distribution and size of the nanoparticles are key parameters to better control the intergrowth characteristics (density, size and distribution) and thus pinning properties. Small nanoparticles (10 to 15 nm) tend to promote short intergrowths and a high density of partial dislocations; however, at high BYTO loads (>10 mol%), large nanoparticles form due to aggregation (50–100 nm) reducing the incoherent interface volume and forming extended defects, which decreases the overall nanostrain [25]. Here, the average nanoparticle size in YBCO-6% BYTO nanocomposites is found to range between 20 and 30 nm, which is slightly higher than the one observed in YBCO-$BaZrO_3$ nanocomposites (10–20 nm), the ones showing the best pinning performances so far in solution-derived films [3,13]. A closer look into the YBCO-6% BYTO local microstructure is shown in Fig. 1(c). It has been observed that randomly oriented nanoparticles are generally surrounded by large clusters of intergrowths forming a dense array of the Y124 phase, where the YBCO (00l) planes are strongly bended.

The combination of high-resolution HAADF and LAADF is particularly useful to visualize and localize the strained region around the partial dislocation associated to the Y124 intergrowths (see more details in Ref. [40]). Figures 2(a) and 2(b) are the HAADF and LAADF images of an isolated ∼25-nm-long Y124 intergrowth, respectively. While the contrast in the HAADF image is uniform over the entire image, the LAADF image presents enhanced contrast at the edges of the intergrowth (pointed by arrows) which encloses the associated Y124 partial dislocations and extend over several YBCO unit cells. Indeed, the presence of the partial dislocation in the YBCO matrix bends the (00l) YBCO planes on either side of the dislocation in order to adapt the extra Cu-O plane thus generating a locally distorted volume which enhances the contrast in the LAADF image. In order to infer the effectiveness of the partial dislocation associated to the Y124 intergrowths as a vortex-pinning agent, the quantification of the lattice deformation is essential and it can be obtained by the geometrical phase analysis tool [41] (GPA). The GPA software is based on the Fourier

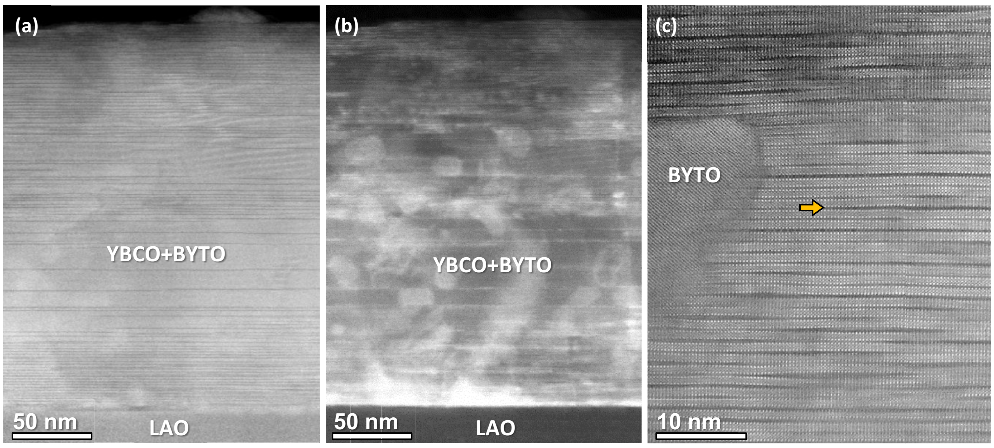

FIG. 1. STEM images of the complex microstructure of YBCO-6% mol BYTO nanocomposite films. Simultaneously acquired HAADF (a) and LAADF (b) low magnification images, showing Y124 intergrowths as dark (in HAADF) and bright (in LAADF) stripes, and embedded Ba_2YTaO_6 nanoparticles (bright spots in LAADF). (c) Closer Z-contrast image from the film bulk showing a YBCO-BYTO interface surrounded by Y124 defects (arrow).

analysis of a high-resolution lattice image selecting a strong Bragg reflection and performing an inverse Fourier transform. The phase component of the resulting complex image gives information on local displacements and rotations of atomic planes compared to an assumed strain-free reference lattice. The strain analysis of a dislocation is shown in Figs. 2(c)–2(e). Figure 2(c) is the HAADF image and Figs. 2(d) and 2(e) are the ε_{yy} and ε_{xx} deformation maps showing the lattice displacements along the $\langle 001\rangle_{\mathrm{YBCO}}$ and $\langle 100\rangle_{\mathrm{YBCO}}$ directions, respectively. Lattice deformation is represented by a color scale which indicates the difference in percentage compared to the reference lattice. The reference lattice is marked in the HAADF image corresponding to a single YBCO unit cell as it is the unity element repeated in the crystal. Two consecutive 90°-rotated images of the same area were taken in order to minimize scan distortions, and only the strain component along the fast scan direction was analyzed from each image. As shown, the most evident lattice deformation is observed in the ε_{yy} map. Notice that the red and green fringes in the ε_{yy} maps put on display the difference between the out-of-plane parameters of the Ba and Y-perovskite blocks in the YBCO [$c_{(\mathrm{Ba\text{-}Y})} = 0.412$ nm and $c_{(\mathrm{Y})} = 0.339$ nm], which corresponds to the distance between the Ba atoms (Cu-O chain layers) and Ba-Y (CuO_2 superconducting planes), respectively. Tensile deformations are observed on the Ba perovskite blocks surrounding the partial dislocation of the intergrowth in the ε_{yy} map. The Cu-O chain layer located at the center of the image, i.e., the plane where the extra Cu-O plane is introduced, undergoes a progressive expansion from the right of the image (reference lattice) towards the left (edge of the dislocation) up to $+4.0 \pm 1.3\%$ (the error is the standard deviation measured in the reference strain-free area). At the same time, the upper and lower nearest Y perovskite blocks to the dislocation are compressed in an asymmetric manner being $-3.8 \pm 1.3\%$ and

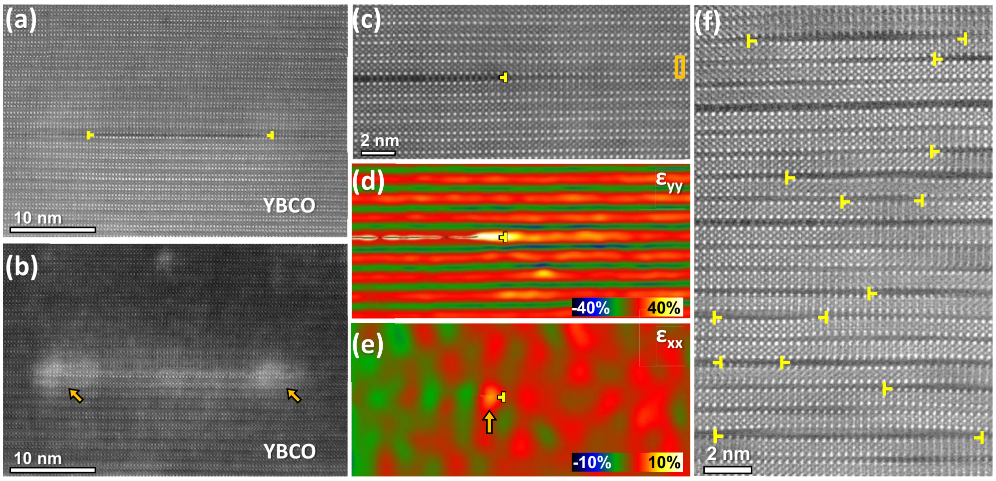

FIG. 2. HAADF (a) and LAADF (b) images of an isolated 25-nm-long Y124 intergrowth. The yellow symbols in the images point to partial dislocations while the arrows to their surrounding strain fields. (c) HAADF image of an Y124 partial dislocation within the YBCO matrix. GPA ε_{yy} (d) and ε_{xx} (e) deformation maps along the $\langle 001\rangle_{\mathrm{YBCO}}$ and $\langle 100\rangle_{\mathrm{YBCO}}$ directions. The Bragg reflections taken for computing the images are the $\{100\}$ and $\{003\}$, respectively. The marked region in the HAADF image is the reference lattice. (f) Enlarged image of the YBCO lattice near the BYTO showing the size and distribution of Y124 defects. Yellow symbols correspond to the partial dislocations associated to Y124.

$-1.7 \pm 1.3\%$, respectively. These compressive deformations gradually vanish away from the dislocation core. On the other hand, the ε_{xx} map shows a $+2.2 \pm 1.1\%$ of tensile deformation located at the partial dislocation core (marked by an arrow in the image), which could induce pair suppression due to localized strain in the YBCO, and thus constituting an effective vortex-pinning center [12] (see line profiles in Ref. [40]).

The strain analysis confirms that the contrast enhancement seen in LAADF images can be interpreted in terms of lattice deformation, and shows that the deformation is found to be highly localized around the partial dislocation. Indeed, recent microscopy studies in combination with density functional theory calculations and image simulations confirmed that this contrast reversal observed between the HAADF and LAADF pair can be attributed to lattice distortion [42]. It is also observed that this local deformation may be extended up to a volume of several nanometers, in agreement with LAADF. Comparing the ε_{yy} and the ε_{xx} maps, it is clear that most of the structural changes in the YBCO due to the lattice deformation are found along the *c* axis and in a lower degree along the *ab* planes. Particularly, tensile strain is found to be confined between BaO planes, i.e., at the Cu-O chain layers. On the contrary, the distances between BaO-Y planes, i.e., CuO superconducting planes, generally remain invariable or slightly compressed in the presence of a high expansion of the Cu-O chains. Indeed, the chains seem to be more playable than the superconducting planes, which may also be related with the fact that oxygen vacancies are more preferable in the Cu-O chains [43,44].

In addition, the strain associated to the Y124 partial dislocations has strong implications on the size and distribution of the intergrowths, as shown in Fig. 2(f), in which short intergrowths, down to 5 nm in some cases, appear staggered in adjacent (00l) planes. Indeed, these strain fields generate local lattice distortions on the surrounding YBCO matrix and tend to interact with each other and with nearby defects, such as twin boundaries (TB). A good example of the last is presented in Fig. 2(e). The ε_{xx} map shows a variation of the in-plane parameter on either side of the intergrowth's edge, a color shift from red to green indicating the presence of a TB. The difference in percentage, $-1.5 \pm 1.1\%$, correlates well with the different *a* and *b* orthorhombic lattice parameters ($a = 0.382$ nm; $b = 0.388$ nm), see Ref. [40] for further details. This reveals that the TB separating the crystal domains is pinned at the dislocation core. $\{110\}$ twinning is another common structural defect in YBCO which in the presence of lattice distortions, as in the case of the Y124 partial dislocations, interact with the dislocations resulting in a break of the vertical boundary coherence and a reduction of the twin spacing [26,27,37]. These structural changes also affect their physical properties [37], as the broken twin boundaries may reduce pinning effectiveness but also flux channeling effects depending on the temperature [27,37].

Yet, another interaction between TBs and Y124 intergrowths takes place when the last run across *a* and *b* crystal domains. The intrinsic stacking fault associated to the double chain in the Y124 implies a dislocation line at the intersection of the TB with the Y124, i.e., along the $\langle 110 \rangle$. Figures 3(a) and 3(b) show the HAADF and LAADF images of an isolated Y124 intergrowth, respectively. Between positions A and B in Fig. 3(a), the $(CuO)_2$ double layer is clearly imaged along the $\langle 010 \rangle$ zone axis, while between B and C along the $\langle 100 \rangle$, denoting the presence of a TB plane at B. As observed in detail in Fig. 3(d) this boundary generates a dislocation and bending of the YBCO planes. This dislocation was previously reported as a Frank sessile type with a ½[110] Burgers vector and a (001) glide plane located between the two Cu-O layers [45]. The strain field around the core is also enhanced in the LAADF image in position *B* due to the YBCO lattice deformation, Fig. 3(b). The ε_{xx} GPA map shows compressive and tensile deformations around the dislocation core, Fig. 3(c), which suggests a nanoscale strained volume along the twin boundary-intergrowth dislocation line, as schematically sketched in Fig. 3(e). Besides, the presence of this dislocation line also induces a break of the twin boundary vertical coherence.

Interestingly, as seen in Fig. 3(b), strain contrast in LAADF is not only enhanced at the dislocations but also along the ab-plane on either side of the intergrowth. This strain contrast is attributed to distortions caused by the presence of randomly distributed complex point defects in the form of Cu and O vacancies buried within the double Cu-O chains of the Y124 intergrowths [39]. Thanks to the short depth of focus of a probe aberration corrected microscope [46], the Cu vacancies can be easily identified in a *Z*-contrast image by the dimmer contrast shown by some Cu sites of the double Cu-O chains when viewed along the [010] direction, as shown in Fig. 4(a) (inset). In a recent work we reported that these defect clusters present a diluted local ferromagnetism that extends to the neighboring CuO_2 superconducting planes [39]. This essentially means that these regions are no longer superconducting and can provide an extra vortex pinning contribution. Yet, these defect clusters also should affect the structure of the surrounding YBCO matrix. To quantify the atomic displacements near the interface between the YBCO matrix and the intergrowth planar defect, a detailed column-to-column spacing analysis has been carried out within the marked area of Fig. 4(a). We have used a center-of-mass refinement method with picometer resolution to calculate the out-of-plane Cu-Cu and Ba-Y interatomic distances. The resulting spacing maps are shown in Fig. 4(b) and 4(c), respectively, where each pixel in the map represents the interplanar distance per atomic row. The corresponding averaged line profiles are plotted in Fig. 4(d). Both profiles show two interplanar distances, which correspond to the different *c*-lattice parameter between CuO_x planes in the $BaCuO_x$ and $YCuO_x$ perovskite blocks [$\text{Cu-Cu}_{(\text{Ba})} = 4.15$ Å; $\text{Cu-Cu}_{(\text{Y})} = 3.39$ Å] and between the Ba-Y and Ba-Ba planes (Ba-Y $= 3.69$ Å; Ba-Ba $= 4.29$ Å), respectively. These reference values are indicated as solid vertical lines in the profiles's graph. As denoted in the maps and profiles, the main deformation takes place in the first YBCO unit cells on either side of the intergrowth, which accounts for the brighter contrast observed in LAADF images, see Fig. 3(b). Indeed, the largest deformations are found in the nearest perovskite blocks to the interface, the ones comprising the $\text{Cu-Cu}_{(\text{Ba})}$, which undergo a tensile deformation up to $+4.7\%$. On the contrary, the $\text{Cu-Cu}_{(\text{Y})}$ compresses about -3.8%. In addition, the spacings comprising Ba and Y cations show a deformation, although lower; in the intergrowth's adjoining YBCO unit cells Ba-Y(1) is compressed about

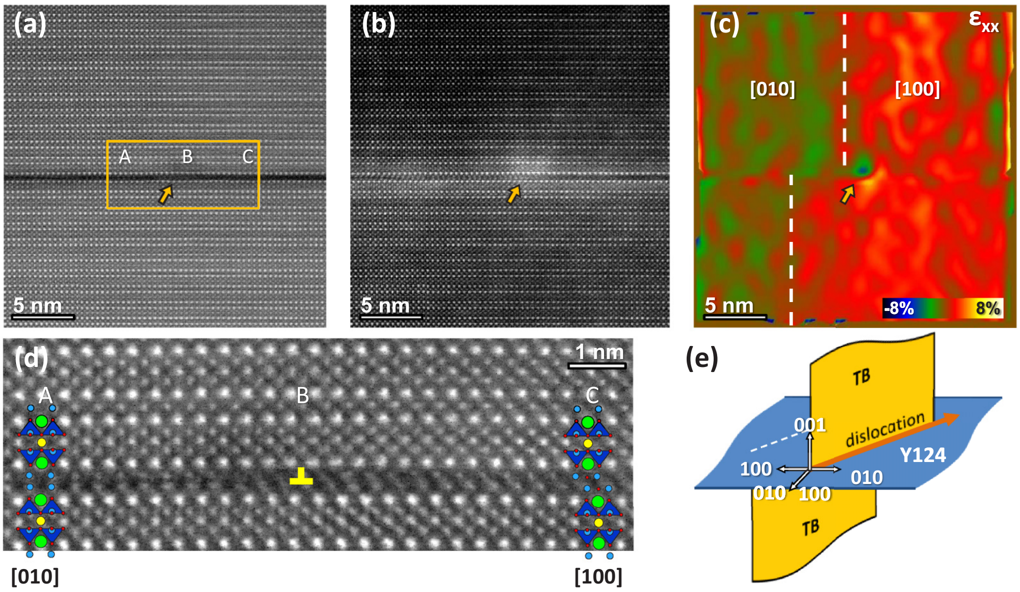

FIG. 3. Simultaneously acquired HAADF (a) and LAADF (b) images of an isolated Y124 intergrowth. When crossing position B, the direction of the chains in the $(CuO)_2$ layer changes from the ⟨010⟩ orientation (position A) into the orthogonal one, the ⟨100⟩ (position C). (c) ε_{xx} GPA deformation map from the HAADF, where the two twin domains are shown by red and green colors. As observed in the LAADF image, lattice distortion is denoted by compressive and tensile strains around the dislocation core. The Bragg reflection taken for computing the image is the $\{100\}_{\mathrm{YBCO}}$. (d) Detailed image of the Frank sessile dislocation on region B with a ½[110] Burgers vector and a (001) glide plane located between the two CuO layers. The YBCO structure is superimposed in the image, where green = Ba, yellow = Y, blue = Cu, and red = O. The yellow symbol marks the position of the dislocation. (e) Sketch of the twin boundary-intergrowth dislocation line.

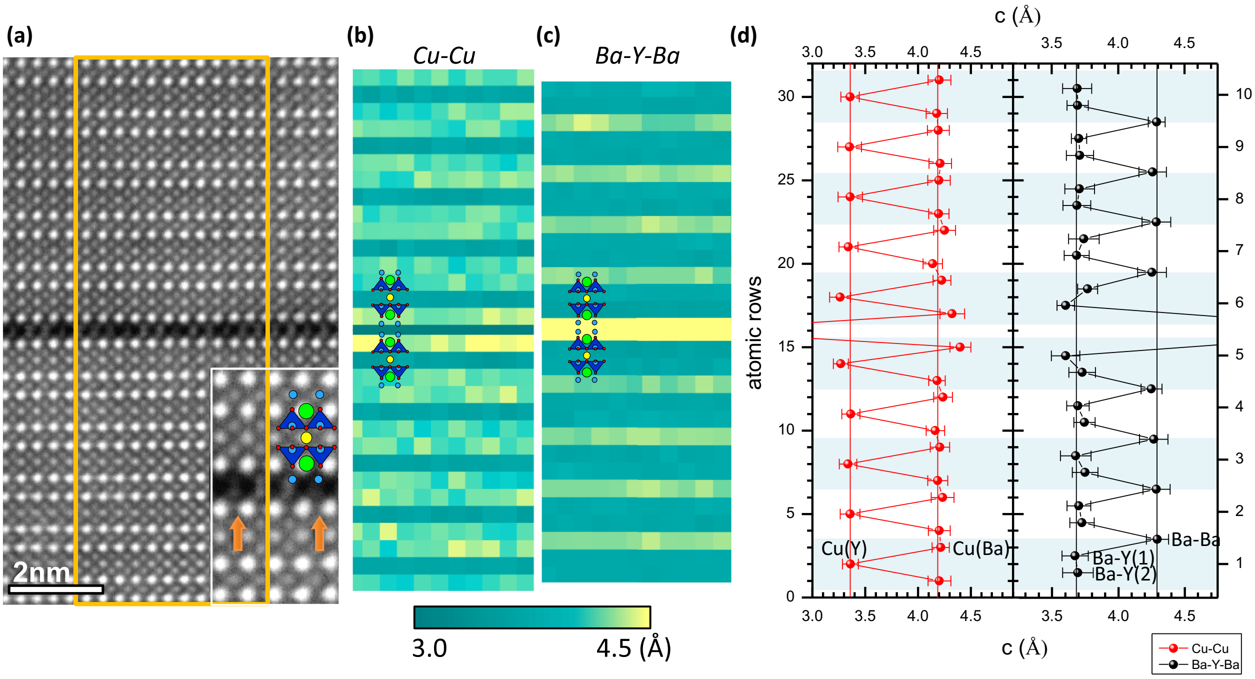

FIG. 4. (a) Atomic resolution image of the Y123 lattice with an Y124 intergrowth imaged along the [010] orientation. The inset shows in detail the faulted double chain, where the arrows point at the Cu vacancies. Cation and oxygen positions are indicated, green = Ba, yellow = Y, blue = Cu, and red = O. Cu-Cu (b) and Ba-Y (c) out-of-plane spacing maps, respectively, calculated from the squared region in (a). (d) Averaged Cu-Cu and Ba-Y distance profiles of the out-of-plane spacing maps in (b) and (c). Distances between de double Cu-O chain layers and between Ba-Ba at the Y124 are out of range for the sake of clarity. Distances were determined by averaging over the 11 unit cells for each atomic row; error bars show standard deviation with respect to averaging for each row. The c-axis parameter is also plotted calculated on the basis of the Cu-Cu distances. The alternation of shadowed areas depicts the sequence of YBCO unit cells.

−1.9% while the complementary, the Ba-Y(2), expands about +1.6%. These results confirm that the major deformations are mainly confined within the contiguous YBCO unit cells, and that the strain fades away gradually in a 5-unit-cell range.

These deformations locally unbalance the YBCO structure near the intergrowth, as well as near the partial dislocation, which should be attributed to the local oxygen and cation deficiency in the structure. In YBCO, the lattice constants are strongly dependent on the oxygen stoichiometry. Also it is known that structural variations along the c axis ultimately determine the superconducting behavior since superconductivity is controlled by the charge transfer between the conducting two-dimensional CuO_2 planes and the Cu-O chains, which act as reservoirs of charge [47]. Then, small changes in the Cu-O bonding due to the deformations may transform the electronic structure of YBCO's CuO_2 superconducting planes [47,48], and thus the physical properties of the films. From the pinning point of view, both structural deformations and point defects are very likely poor superconducting regions (decrease of superconducting order parameter), and their particular vortex pinning behavior must be evaluated in further works.

IV. SUMMARY AND CONCLUSIONS

In summary, we observed that the complex microstructure of YBCO nanocomposite thin films stems from the interplay between defects. Using different STEM imaging modes in combination with local strain analyses of atomic-resolution images, we confirmed that the nucleation of the Y124 intergrowth sets off a chain reaction of self-assembling and strain-driven interactions that profoundly transform the defect landscape that ultimately determine the physical properties of the YBCO films. To this aim, controlling the size and distribution of embedded nanoparticles is a crucial task for the homogeneous distribution of a high density of Y124 intergrowths and tunes the defects characteristics in the films to design superconducting nanocomposites with specific physical properties.

ACKNOWLEDGMENTS

Authors acknowledge financial support from Spanish Ministry of Economy and Competitiveness through the "Severo Ochoa" Programme for Centres of Excellence in R&D (SEV-2015-0496), CONSOLIDER Excellence Network (MAT2015-68994-REDC), COACHSUPENERGY project (MAT2014-51778-C2-1-R, co-financed by the European Regional Development Fund), European Research Council Advanced Grant Award ERC-2014-ADG-669504, and from the Catalan Government with 2014-SGR-753 and Xarmae. J.G. and M.C. acknowledge Ramon y Cajal Program (RyC-2012-11709 and RYC-2013-12448, respectively). The microscopy work were conducted in the Laboratorio de Microscopias Avanzadas at Instituto de Nanociencia de Aragon - Universidad de Zaragoza (Zaragoza, Spain). Authors acknowledge the LMA-INA for offering access to their instruments and expertise.

---

[1] B. Dam, J. M. Huijbregtse, F. C. Klaassen, R. C. F. van der Geest, G. Doornbos, J. H. Rector, A. M. Testa, S. Freisem, J. C. Martinez, B. Stauble-Pumpin, and R. Griessen, Nature (London) **399**, 439 (1999).

[2] D. Larbalestier, A. Gurevich, D. M. Feldmann, and A. Polyanskii, Nature (London) **414**, 368 (2001).

[3] J. Gutiérrez, A. Llordés, J. Gázquez, M. Gibert, N. Romà, S. Ricart, A. Pomar, F. Sandiumenge, N. Mestres, T. Puig, X. Obradors, J. Gutierrez, A. Llordes, J. Gazquez, and N. Roma, Nat. Mater. **6**, 367 (2007).

[4] S. R. Foltyn, L. Civale, J. L. Macmanus-Driscoll, Q. X. Jia, B. Maiorov, H. Wang, and M. Maley, Nat. Mater. **6**, 631 (2007).

[5] A. Goyal, S. Kang, K. J. Leonard, P. M. Martin, A. A. Gapud, M. Varela, M. Paranthaman, A. O. Ijaduola, E. D. Specht, J. R. Thompson, D. K. Christen, S. J. Pennycook, and F. A. List, Supercond. Sci. Technol. **18**, 1533 (2005).

[6] K. Matsumoto and P. Mele, Supercond. Sci. Technol. **23**, 014001 (2010).

[7] J. L. Macmanus-Driscoll, S. R. Foltyn, Q. X. Jia, H. Wang, A. Serquis, L. Civale, B. Maiorov, M. E. Hawley, M. P. Maley, and D. E. Peterson, Nat. Mater. **3**, 439 (2004).

[8] T. Haugan, P. N. Barnes, R. Wheeler, F. Meisenkothen, and M. Sumption, Nature (London) **430**, 867 (2004).

[9] G. Blatter, M. V Feigelman, V. B. Geshkenbein, A. I. Larkin, and V. M. Vinokur, Rev. Mod. Phys. **66**, 1125 (1994).

[10] A. Pomar, V. R. Vlad, A. Llordés, A. Palau, J. Gutiérrez, S. Ricart, T. Puig, X. Obradors, and A. Usoskin, IEEE Trans. Appl. Supercond. **19**, 3258 (2009).

[11] V. Selvamanickam, Y. Chen, T. Shi, Y. Liu, N. D. Khatri, J. Liu, Y. Yao, X. Xiong, C. Lei, S. Soloveichik, E. Galstyan, and G. Majkic, Supercond. Sci. Technol. **26**, 035006 (2013).

[12] G. Deutscher, Appl. Phys. Lett. **96**, 122502 (2010).

[13] A. Llordés, A. Palau, J. Gázquez, M. Coll, R. Vlad, A. Pomar, J. Arbiol, R. Guzmán, S. Ye, V. Rouco, F. Sandiumenge, S. Ricart, T. Puig, M. Varela, D. Chateigner, J. Vanacken, J. Gutiérrez, V. Moshchalkov, G. Deutscher, C. Magen, and X. Obradors, Nat. Mater. **11**, 329 (2012).

[14] S. Engel, T. Thersleff, R. Huhne, L. Schultz, and B. Holzapfel, Appl. Phys. Lett. **90**, 102505 (2007).

[15] M. Erbe, J. Hänisch, R. Hühne, T. Freudenberg, A. Kirchner, L. Molina-Luna, C. Damm, G. Van Tendeloo, S. Kaskel, L. Schultz, and B. Holzapfel, Supercond. Sci. Technol. **28**, 114002 (2015).

[16] L. Molina-Luna, M. Duerrschnabel, S. Turner, M. Erbe, G. T. Martinez, S. Van Aert, B. Holzapfel, and G. Van Tendeloo, Supercond. Sci. Technol. **28**, 115009 (2015).

[17] T. Puig, J. Gutiérrez, A. Pomar, A. Llordés, J. Gázquez, S. Ricart, F. Sandiumenge, X. Obradors, J. Gutierrez, A. Llordes, and J. Gazquez, Supercond. Sci. Technol. **21**, 034008 (2008).

[18] I. Bretos, T. Schneller, M. Falter, M. Bäcker, E. Hollmann, R. Wordenweber, L. Molina-Luna, G. Van Tendeloo, and O. Eibl, J. Mater. Chem. C **3**, 3971 (2015).

[19] S. Ye, H. Suo, Z. Wu, M. Liu, Y. Xu, L. Ma, and M. Zhou, Phys. C Supercond. Its Appl. **471**, 265 (2011).

[20] K. Konya, K. Ootaguro, T. Nishiyama, R. Teranishi, T. Kiss, K. Yamada, K. Kaneko, M. Yoshizumi, and T. Izumi, Phys. C Supercond. Its Appl. **494**, 144 (2013).

[21] M. Coll, S. Ye, V. Rouco, A. Palau, R. Guzman, J. Gazquez, J. Arbiol, H. Suo, T. Puig, and X. Obradors, Supercond. Sci. Technol. **26**, 015001 (2013).

[22] T. Honjo, Y. Nakamura, R. Teranishi, H. Fuji, J. Shibata, and T. Izumi, IEEE Trans. Appiled Supercond. **13**, 2516 (2003).

[23] M. Miura, B. Maiorov, J. O. Willis, T. Kato, M. Sato, T. Izumi, Y. Shiohara, and L. Civale, Supercond. Sci. Technol. **26**, 035008 (2013).

[24] H. Horita, R. Teranishi, K. Yamada, K. Kaneko, Y. Sato, K. Otaguro, T. Nishiyama, T. Izumi, and S. Awaji, Supercond. Sci. Technol. **30**, 025022 (2017).

[25] M. Coll, R. Guzman, P. Garcés, J. Gazquez, V. Rouco, A. Palau, S. Ye, C. Magen, H. Suo, H. Castro, T. Puig, and X. Obradors, Supercond. Sci. Technol. **27**, 044008 (2014).

[26] P. Mele, R. Guzman, J. Gazquez, T. Puig, X. Obradors, S. Saini, Y. Yoshida, M. Mukaida, A. Ichinose, K. Matsumoto, and M. Idries Adam, Supercond. Sci. Technol. **28**, 024002 (2015).

[27] V. Rouco, A. Palau, R. Guzman, J. Gazquez, M. Coll, X. Obradors, and T. Puig, Supercond. Sci. Technol. **27**, 125009 (2014).

[28] S. J. Pennycook and D. E. Jesson, Ultramicroscopy **37**, 14 (1991).

[29] P. J. Phillips, M. De Graef, L. Kovarik, A. Agrawal, W. Windl, M. J. Mills, and M. De Graef, Ultramicroscopy **116**, 47 (2012).

[30] D. A. Muller, N. Nakagawa, A. Ohtomo, J. L. Grazul, and H. Y. Hwang, Nature (London) **430**, 657 (2004).

[31] V. Grillo and F. Rossi, J. Cryst. Growth **318**, 1151 (2011).

[32] J. M. Cowley and Y. Huang, Ultramicroscopy **40**, 171 (1992).

[33] H. W. Zandbergen, R. Gronsky, K. Wang, and G. Thomas, Nature (London) **331**, 596 (1988).

[34] A. F. Marshall, R. W. Barton, K. Char, A. Kapitulnik, B. Oh, R. H. Hammond, and S. S. Laderman, Phys. Rev. B **37**, 9353 (1988).

[35] G. Vantendeloo and S. Amelinckx, J. Electron Microsc. Tech. **8**, 285 (1988).

[36] R. Ramesh, D. M. Hwang, T. Venkatesan, T. S. Ravi, L. Nazar, A. Inam, X. D. Wu, B. Dutta, G. Thomas, A. F. Marshall, and T. H. Geballe, Science **247**, 57 (1990).

[37] R. Guzman, J. Gazquez, V. Rouco, A. Palau, C. Magen, M. Varela, J. Arbiol, X. Obradors, and T. Puig, Appl. Phys. Lett. **102**, 081906 (2013).

[38] J. Tafto, M. Suenaga, and R. L. Sabatini, Appl. Phys. Lett. **52**, 667 (1988).

[39] J. Gazquez, R. Guzman, R. Mishra, E. Bartolomé, J. Salafranca, C. Magén, M. Varela, M. Coll, S. M. Valvidares, P. Gargiani, E. Pellegrin, J. Herrero-martin, S. J. Pennycook, S. T. Pantelides, T. Puig, and X. Obradors, Adv. Sci. **201500295**, 1 (2016).

[40] See Supplemental Material at http://link.aps.org/supplemental/10.1103/PhysRevMaterials.1.024801 for more details in the microstructure of the films and strain analysis of defects.

[41] M. J. Hÿtch, E. Snoeck, and R. Kilaas, Ultramicroscopy **74**, 131 (1998).

[42] L. Wu, Q. Meng, C. Jooss, J. C. Zheng, H. Inada, D. Su, Q. Li, and Y. Zhu, Adv. Funct. Mater. **23**, 5728 (2013).

[43] J. D. Jorgensen, M. A. Beno, D. G. Hinks, L. Soderholm, K. J. Volin, R. L. Hitterman, J. D. Grace, I. K. Schuller, C. U. Segre, K. Zhang, and M. S. Kleefisch, Phys. Rev. B **36**, 3608 (1987).

[44] S. J. Rothman, J. L. Routbort, U. Welp, and J. E. Baker, Phys. Rev. B **44**, 2326 (1991).

[45] G. Vantendeloo, T. Krekels, and S. Amelinckx, Philos. Mag. Lett. **63**, 189 (1991).

[46] S. J. Pennycook and P. D. Nellist, *Scanning Transmission Electron Microscopy: Imaging and Analysis* (Springer-V, New York, 2011).

[47] J. D. Jorgensen, B. W. Veal, A. P. Paulikas, L. J. Nowicki, G. W. Crabtree, H. Claus, and W. K. Kwok, Phys. Rev. B **41**, 1863 (1990).

[48] E. S. Božin, A. Huq, B. Shen, H. Claus, W. K. Kwok, and J. M. Tranquada, Phys. Rev. B **93**, 054523 (2016).